THE ASTROPHYSICAL JOURNAL, 421:738–752, 1994 February 1

THE TIME-DELAY SPECTRUM OF GX 5−1 IN ITS HORIZONTAL BRANCH

B. VAUGHAN,[1] M. VAN DER KLIS,[1] W. H. G. LEWIN,[2] R. A. M. J. WIJERS,[3] J. VAN PARADIJS,[1]
T. DOTANI,[4] AND K. MITSUDA[4]

Received 1993 April 12; accepted 1993 August 9

ABSTRACT

Using a cross-spectral technique we investigate time delays between intensity variations of GX 5−1 in 10 X-ray spectral channels. The data were taken during a 1989 *Ginga* observation during which the source was in its horizontal-branch spectral state. We develop a new method to measure "time-delay spectra" in fixed Fourier frequency ranges and use it to determine the energy and intensity dependence of time delays in the low-frequency noise ($\nu < 2$ Hz), the horizontal branch QPO, and the QPO second harmonic. These are the first time-delay spectra of a *Z*-source in its horizontal branch, and the first detection of time delays in the second harmonic. We find that

1. In the low-frequency noise, intensity variations at low energies lag those at high energies by tens of milliseconds; the lag increases with energy.
2. High-energy photons lag low-energy photons by up to 4 ms, not only at the QPO first harmonic frequency but also in the second harmonic. In both harmonics, the lag increases with energy.
3. Delays are *not* monotonically related to QPO frequency. The time delays are longest at the low-intensity, low-QPO frequency end of the horizontal branch, and decrease as the intensity increases and the source moves along the horizontal branch toward the normal branch vertex; they increase again near the vertex.
4. The time-delay spectra of the QPO first and second harmonic are similar but they are not identical.
5. Intensity variations in the different spectral channels are correlated with one another.

We consider two mechanisms for the production of the time lags: Comptonization and evolving shots. We perform Monte Carlo simulations of Compton scattering in a homogeneous, isotropic, central corona and show that it can qualitatively explain the observed energy and time-delay spectra, but that it cannot explain the differences in the QPO first and second harmonic time-delay spectra, nor the observed dependence of the QPO fractional rms variability upon energy. We consider implications of our results for millisecond pulsar searches in low-mass X-ray binaries.

Subject headings: pulsars: general — stars: individual (GX 5−1) — X-rays: stars

1. INTRODUCTION

Following the discovery of rapid intensity-dependent quasi-periodic oscillations, or QPO, in the X-ray light curves of the bright low-mass X-ray binaries GX 5−1 (van der Klis et al. 1985a, b) Cyg X-2 (Hasinger et al. 1985, 1986; Norris & Wood 1985), and Sco X-1 (Middleditch & Priedhorsky 1985, 1986; van der Klis et al. 1985c), it quickly became clear that at least two and possibly three classes of QPO behavior occurs in these sources whose occurrence corresponds to X-ray spectral state. See Lewin, van Paradijs & van der Klis (1988), and van der Klis (1989a, 1993) for reviews of QPO and LMXB. Spectral state is defined by a point in a color-color diagram. The *x*-axis gives the ratio of the count rate at low energies (typically 1–3 keV) to intermediate energies (typically 3–6 keV), and the *y*-axis gives the ratio of the count rate at high energies (typically 6–12 keV) to intermediate energies. As the spectrum varies in time, this point moves through the diagram, tracing out a characteristic pattern. The instantaneous position of the source in the diagram defines its spectral state. Bright low-mass X-ray binaries can be divided into two groups on the basis of their correlated color-color diagram and QPO behavior: *Z* sources and atoll sources (Hasinger & van der Klis 1989). *Z* sources, of which GX 5−1 is one of six known examples, are characterized by spectral variability with the property that the points in color-color diagrams fall on *Z*-shaped curves.

The upper limb of the *Z* is referred to as the horizontal branch. Power spectra taken when a *Z* source is in the horizontal branch show a peak in the range 13–55 Hz with a FWHM of order 5–10 Hz. We refer to such horizontal-branch QPO as horizontal-branch oscillations, or HBO. The HBO vary with source intensity, generally increasing in Fourier frequency and decreasing in fractional root mean square (rms) amplitude as the intensity increases. A second peak, identified as the harmonic of the HBO, has been observed in power spectra of GX 5−1 (Dotani 1988; Lewin et al. 1992), GX 17+2 (Penninx et al. 1990) and possibly Cyg X-2 (Hasinger 1987). We call the fundamental peak the first harmonic and the harmonic, at twice the frequency of the fundamental peak, we call the second harmonic. The existence of the second harmonic peak implies that modulations in the source intensity are not sinusoidal. In addition to the HBO first and second harmonic peaks, three noise features are seen in all horizontal-branch power spectra (van der Klis et al. 1987; Hasinger, Preidhorsky, & Middleditch 1989; Hasinger & van der Klis 1989). A very low frequency noise term well described by a power-law dominates

[1] Astronomical Institute "Anton Pannekoek," University of Amsterdam, Center for High-Energy Astrophysics, Kruislaan 403, 1098 SJ Amsterdam, The Netherlands.
[2] Massachusetts Institute of Technology, Center for Space Research, Room 37-627, Cambridge, MA 02139.
[3] Princeton University, 124 Peyton Hall, Princeton, NJ 08544.
[4] Institute of Space and Astronautical Science, 3-1-1 Yoshinodai, Sagamihara, Kanagawa 229, Japan.

the power spectrum around 1 Hz. An additional component referred to as low-frequency noise is evident above a few tenths of a Hertz and dominates the power spectrum around 1 Hz. Finally, there is broad-band high-frequency noise the can usually be described by a relatively flat power-law multiplying an exponential function with a cutoff frequency of 30–70 Hz (Hasinger & van der Klis 1989). In some cases there is no evidence for a cutoff in the high-frequency noise.

Shot models for HBO (Lamb et al. 1985; Shibazaki & Lamb 1987; Shibazaki, Elsner, & Weisskopf 1987; Shibazaki et al. 1988) postulate that blobs of matter, called clumps, fall onto the neutron star, and that accretion from the clumps is modulated at the HBO frequency. The enhancements in X-ray intensity caused by the clumps are referred to as shots. The shots form an envelope function for the modulations. The low-frequency noise is the power spectral signature of the shots, and the HBO peak is the signature of the modulations.

At its right, high-intensity end, the horizontal branch connects with the diagonal limb of the Z, which is referred to as the normal branch. On the normal-branch, spectral hardness is correlated with source intensity. Normal-branch oscillations with centroid frequencies near 6 Hz are seen in normal-branch power spectra of all Z sources (Hasinger & van der Klis 1989). Normal-branch power spectra contain no low-frequency noise. Very low-frequency noise, however, is seen on all spectral branches.

The normal branch connects at its spectrally soft end with the flaring branch. The QPO frequency increases and the rms amplitude decreases as the source moves up the flaring branch (flaring-branch QPO have been observed near the normal-branch vertex). A flaring branch has never been observed in GX 5−1. Evidence for a new spectral branch connected to the lower normal branch has recently been found in *EXOSAT* data from GX 5−1 and may be the previously unseen flaring branch (Kuulkers et al. 1993). It is thought that the mass accretion rate, $\dot{M}$, onto the neutron star increases as the source moves along the Z track in the color-color diagram from the horizontal to the normal and finally to the flaring branch (Vrtilek et al. 1990, 1991; Hasinger et al. 1990). See Lewin, van Paradijs, & van der Klis (1988), Lamb (1988), Hasinger (1988), or van der Klis (1989a, b) for reviews of QPO phenomenology and models.

Hasinger (1987) measured a delay of $\sim$3 ms between high- and low-energy light curves of Cyg X-2 obtained on the horizontal branch, using a cross-correlation function. For the purposes of this paper, photons of order 1–5 keV are called soft. Hard photons have energies above 5 keV. Van der Klis et al. (1987) found similarly that high-energy photons lag low-energy photons by a few milliseconds in the neighborhood of the HBO Fourier frequency in light curves of Cyg X-2 and GX 5−1 obtained on the horizontal branch, using a complex cross spectrum. At frequencies where low-frequency noise dominates the power spectrum, the high-energy photons lead the low-energy photons. The high-energy lag in the HBO was seen to decrease as the source moved up the horizontal branch and the QPO frequency increased. It was speculated that Comptonization in a central corona was responsible for the lags (Hasinger 1987; van der Klis et al. 1987).

Shortly after the time delay results were published, three groups published the results of Monte Carlo simulations of scattering in a homogeneous central corona (Wijers et al. 1987; Stollman et al. 1987; Bussard et al. 1988). They found that millisecond high-energy photon time delays can be made consistent with cloud parameters that can simultaneously reproduce observed low-mass X-ray binary energy spectra. It was predicted that the high-energy photon time delay should increase with energy. More recently, Schulz & Wijers (1992) have shown that it is possible to fit the energy spectra of a number of low-mass X-ray binaries, including GX 5−1, all along their horizontal, normal, and flaring-branches with a Compton model using only three parameters: input blackbody temperature, cloud optical depth, and cloud temperature. Wijers et al. (1987) also found that for some values of the input spectrum temperature and cloud Compton temperature and optical depth, photons near 1 keV arrive prior to both higher and lower energy photons, so that there is a minimum in the modeled time-delay spectra.

Until recently, it was only possible to measure time delays between pairs of energies, as high time resolution data in more than two spectral channels were either unavailable or had low count rates that required rebinning the data into two broad spectral channels to see the delays. Observers and modelers each remarked in their papers that multichannel measurements of time delays may help illuminate the physics of inner accretion disks. In this paper, we develop a new, sensitive method for measuring multichannel time delays in weak signals. We measure complex cross spectra between all pairs of spectral channels and average over data segments. The method exploits the fact that cross spectral measurements are dominated by counting noise. Uncertainties in the average cross spectrum for each pair of channels are thus independent, and we can find a best fit using a χ^2 minimization technique. Applying the new method, we report for the first time the energy dependence of the time delays in GX 5−1 on the horizontal branch and the detection of time delays in the HBO second harmonic. We study the dependence of the "time-delay spectra" on source intensity, compare the time-delay spectrum at the HBO first and second harmonic frequencies, and discuss implications to models of X-ray production in low-mass X-ray binaries, and to sensitivity limits in pulsar searches.

2. OBSERVATIONS

During 5 days in 1989, the Large Area Counter (LAC) on *Ginga* (Makino et al. 1987; Turner et al. 1989) was used to perform a high time resolution multispectral channel observation of GX 5−1. The observation was performed using the MPC-3 data mode at high time resolution, in which the counts in 12 spectral channels in the range 1–37 keV are recorded every 8 ms. For timing analysis the data are rebinned into 10 channels. During 4 days of the observation, GX 5−1 was in the horizontal branch. The total raw count rate (all spectral channels summed) on the horizontal branch was between 3300 and 9500 counts s^{-1}. HBO with frequencies from a record low of 13 through 50 Hz were observed. A full report on the dependences of the general QPO and noise characteristics on the X-ray spectral state has been given by Lewin et al. (1992), to whose paper we refer frequently for QPO centroid frequency and rms amplitude values.

3. ANALYSIS

3.1. *Best-fit Time-Delay Spectra*

The complex cross-spectrum is the method of choice for measuring small time delays between signals. The Fourier transform of the cross-correlation function, and hence containing the same information, the complex cross spectrum has the advantage that is measures time delay as a function of Fourier

frequency, and that no fitting or peak searching is required to identify and measure time delays. First applied in X-ray astronomy to *Z* source QPO data in only two spectral channels (van der Klis et al. 1987), it has since been used to measure time delays between a larger number of energy channels. We shall call the results of such measurements *time-delay spectra.* The traditional way to measure time-delay spectra has been to measure all time delays with respect to one reference spectral channel, typically the channel with the largest flux. Thus, give N_c spectral channels, measure $N_c - 1$ cross spectra. All time delays are quoted with respect to the reference channel. For our analysis, we have used a new, more sensitive, and symmetric method that does not rely upon an individual reference channel, but instead makes use of all available information.

In the following discussion we will consistently use a superscript tilde ($\tilde{}$) to indicate a quantity determined with a single measurement, no averaging. A hat ($\hat{}$) above a quantity denotes an average over independent data segments and/or Fourier frequencies. Intrinsic quantities, such as the intrinsic signal powers will have no accent. These intrinsic quantities of course are what we are trying to estimate. Values determined using χ^2 minimization are indicated with the superscript "fit."

Time series data in N_c energy spectral channels are divided into N_s independent segments each of length T seconds and containing N time bins of length T/N. Let the number of photons in time bin k of segment p in spectral channel m be $\tilde{x}_{mp}(t_k)$, where t_k is the start time of the kth bin. For each segment and in each spectral channel, calculate the Fourier coefficient $\tilde{X}_{mp}(\nu_j)$;

$$\tilde{X}_{mp}(\nu_j) = \sum_{k=1}^{N} \tilde{x}_{mp}(t_k) e^{2\pi i jk/N} . \tag{1}$$

The Fourier frequency, ν_j, is j/T, and $i = (-1)^{1/2}$. The Fourier cross amplitude between spectra channels m and n at frequency ν_j is defined to be

$$G_{mn}(\nu) \equiv \lim_{T\to\infty} E[X_m^*(\nu, T) X_n(\nu, T)] . \tag{2}$$

An asterisk denotes complex conjugation, E indicates an average over an ensemble of statistically independent measurements, and $X_m(\nu, T)$ is defined as

$$X_m(\nu, T) = \int_0^T x_m(t) e^{2\pi i \nu t} dt , \tag{3}$$

where $x_m(t)$ is the instantaneous count rate at time t in spectral channel m. Note that although we refer to $G_{mn}(\nu_j)$ as the cross amplitude, it is a complex quantity. We estimate the cross amplitude at frequency ν_j by averaging over independent segments:

$$\hat{G}_{mn}(\nu_j) = \frac{1}{N_s} \sum_{p=1}^{N_s} \tilde{X}_{mp}^*(\nu_j) \tilde{X}_{np}(\nu_j) . \tag{4}$$

The complex cross spectrum is defined as the Fourier cross amplitude as a function of Fourier frequency.

To obtain the average cross amplitude of the HBO we average over the Fourier frequency range, or some part of the Fourier frequency range, of the HBO, in addition to averaging over independent data segments. Let us average from ν_- to ν_+. We indicate the frequency-averaged cross amplitude of the HBO by $\hat{G}_{mn}$,

$$\hat{G}_{mn} = \frac{1}{T\Delta\nu} \sum_{\nu=\nu_-}^{\nu_+} \hat{G}_{mn}(\nu_j) , \tag{5}$$

where the frequency range has width $\Delta\nu = \nu_+ - \nu_-$ and contains $T\Delta\nu$ Fourier frequency channels. Similarly, we define the intrinsic cross amplitude of the HBO to be

$$G_{mn} \equiv \frac{1}{\Delta\nu} \int_{\nu_-}^{\nu_+} G_{mn}(\nu) d\nu , \tag{6}$$

For a stationary and Gaussian, or nearly Gaussian, random process, in the limit of large N_s, $\hat{G}_{mn}$ approaches G_{mn} (Bendat & Piersol 1986):

$$\lim_{N_s\to\infty} \hat{G}_{mn} = G_{mn} . \tag{7}$$

If we substitute equation (2) into equation (6), we see that G_{mn} is the mean, over the HBO peak frequency range, of the product $X_m^*(\nu) X_n(\nu)$. If the relative phases of the signals are constant or nearly constant over the Fourier frequency range averaged, the mean value of the product is approximately equal to the product of the mean values, and we can express the intrinsic cross amplitude as the product of intrinsic Fourier coefficients;

$$G_{mn} = X_m^* X_n . \tag{8}$$

The phase of the cross-spectrum measures the phase difference between the Fourier coefficients in spectral channels m and n as a function of Fourier frequency. We define phase on the interval $[-\frac{1}{2}, \frac{1}{2}]$, and hence the phase difference is given by

$$\delta\phi_{mn}(\nu_j) = \frac{1}{2\pi} \arg [G_{mn}(\nu_j)] . \tag{9}$$

To measure time delays in the HBO, we divide the phase of the average Fourier cross amplitude by the average Fourier frequency of the HBO.

With N_c spectral channels it is possible to calculate $N_c(N_c - 1)/2$ different average cross amplitudes, one for each pair of spectral changes. For noise signals such as the ones we are dealing with here, averaging a large number of independent data segments and Fourier frequencies results in an essential statistical independence of each of the $N_c(N_c - 1)/2$ average cross amplitudes. We have developed a χ^2 technique to utilize all $N_c(N_c - 1)/2$ cross spectra simultaneously to determine a best fit time-delay spectrum. In this section we only give an outline of our method. Details of implementation and uncertainty estimation are discussed in the Appendix.

The underlying physical quantities we wish to estimate are intrinsic Fourier coefficients X_n for each energy channel, which in various combinations through equation (2) yield $N_c(N_c - 1)/2$ intrinsic cross amplitudes.

By measuring $N_c(N_c - 1)/2$ average cross spectra $\hat{G}_{mn}$, we obtain $N_c(N_c - 1)/2$ statistically independent estimates of the products of intrinsic Fourier coefficients $X_m^* X_n$. If N_c is greater than three, the number of measured cross spectra exceeds the number of spectral channels. In this case we can determine values of the Fourier coefficients that best fit the observed average cross spectra, defining best fit in the χ-squared sense. Specifically, we define χ^2 as

$$\chi^2 \equiv \sum_{m<n} \frac{|X_m^{\text{fit}*} X_n^{\text{fit}} - \hat{G}_{mn}|^2}{\sigma_{mn}^2} , \tag{10}$$

and minimize χ^2 to find best-fit values of the intrinsic Fourier coefficients. We show in the Appendix that in the case of Gaussian statistics and a Poisson-dominated signal (which is

our present regime), the variance is approximately given by

$$\sigma_{mn}^2 = \frac{\hat{G}_{mm}\hat{G}_{nn}}{2n_d}, \quad (11)$$

where n_d is the total number of measurements used to obtain the average; $n_d = N_s T\Delta\nu$. Because we typically average of order 10^4 measurements to obtain an estimate of each G_{mn}, the Gaussian approximation can be expected to be very good. Note that the derivation in the Appendix uses equivalent but more mathematically elegant transfer functions instead of intrinsic Fourier coefficients.

By minimizing χ^2 we obtain a best-fit value for the average Fourier coefficient of the HBO in each spectral channel. The phase delays between the channels can be read off from the phases of the coefficients. We thus obtain a χ^2 best-fit time-delay spectrum. It should be stressed that because cross spectra measure only phase differences, we do not measure absolute phases with the χ^2 method, only differences.

Note that although we quote time delays and uncertainties relative to a particular spectral channel, simply because we must choose some zero level, the χ^2 technique uses no preferred spectral channel in determining the delays. The relative values of the phases are invariant to the choice of zero level.

The method assumes that the intrinsic signal in each energy channel in the Fourier frequency range under investigation resembles that in the other energy channels up to a shift in phase and a scaling in amplitude, a property called "coherence." The value of χ^2 provides a measure of the extent to which this assumption is in accordance with the data; in our case the assumption turns out to be a very good one. If the signals are not coherent, the method will measure the time lags between the coherent parts of the signals, and the reduced χ^2 value will exceed unity.

We checked that the results we obtained using our new method are entirely consistent with those obtained using the traditional approach with one reference channel. Our method produces more tightly constrained values for the time lags.

Because the method outlined here is new, we performed numerical simulations with simulated signals and noise to test our mathematical results. We found that we could determine both the time delays and strengths of the simulated signals through the phases and amplitudes, respectively, of the best-fit Fourier coefficients.

3.2. *Coherence Spectra*

The best-fit Fourier coefficients described in the previous subsection can be converted to Fourier powers in the manner of standard Fourier coefficients:

$$G_{mn}^{\rm fit} = X_m^{\rm fit*} X_m^{\rm fit}. \quad (12)$$

Because best-fit Fourier coefficients are found using cross spectra which are sensitive only to coherent signals, the power in spectral channel m found using equation (12) is a measure of the average signal power in channel m at the HBO frequency that is coherent with all of the other spectral channels. We call $G_{mm}^{\rm fit}$ the *correlated power*. The ratio of the correlated power in channel m to the total intrinsic power in channel m (Poisson noise subtracted) is the mean squared fraction of the QPO signal that the coherent with the signals in the other channels. We define

$$\gamma_m^2 = \frac{G_{mm}^{\rm fit}}{P_m}, \quad (13)$$

where P_m is the signal power averaged over the QPO with Poisson noise subtracted. γ_m^2 is the intrinsic coherence (Vaughan 1991). The intrinsic coherence, γ_m^2 is defined such that a value of unity indicates perfect coherence, and a value of zero indicates a complete a complete lack of coherence. We define the *coherence spectrum* to be the intrinsic coherence found using equation (13), as a function of energy. If the coherence, corrected as in equation (13) for Poisson noise, is unity for all spectral channels, we can conclude that the signal in each channel is the same as in each other channel up to a phase shift and amplitude scaling; a strong indication that the same physical process underlies the signal in each channel. A reduced χ^2 value consistent with unity is also an indication that the signals are the same up to the phase and amplitude factor. The coherence, γ_m^2, provides a measure of the coherence separately for each spectral channel relative to the others, where the value of χ^2 provides a measure for the entire data set.

4. RESULTS

4.1. *HBO Time-Delay Spectra*

The HBO properties in GX 5−1 are strongly correlated with color-color diagram position, and hence with source intensity. In Lewin et al. (1992), the dependence of horizontal-branch power spectral characteristics such as HBO frequency and HBO and low-frequency noise fractional rms amplitude are discussed in detail for the same data set we have analyzed. We present a summary of the HBO properties in the following paragraph.

Figure 1 shows a hardness-intensity diagram of the horizontal-branch data we have analyzed. At the low-intensity end the QPO frequency is as low as 13 Hz, the lowest HBO frequency ever observed (Lewin et al. 1992), with fractional rms variability as high as 7.5% in the 1–18 keV channel. A second harmonic peak is seen in all cases for which it is below the Nyquist frequency of 64 Hz. See Figure 2 for a sample power spectrum. The HBO first harmonic peak at 13 Hz is clearly visible. The HBO second harmonic peak at 26 Hz appears as a shoulder in the power spectrum. HBO frequency increases with intensity. At its high-intensity end the horizontal branch connects with the normal branch. Near the normal branch vertex the HBO frequency approaches 50 Hz and the fractional rms variability of the HBO is only ~3% (1–18 keV). We divided the horizontal branch into 10 regions on the basis of source intensity. These regions are indicated in Figure 1, along with the HBO frequency and fractional rms amplitude in each region.

We measured time-delay spectra in each horizontal-branch intensity region for the HBO first harmonic, and for the second harmonic when the Nyquist frequency permitted (regions 1–4), averaging data within the FWHM of the HBO first or second harmonic peak in each region. As the source moved up the horizontal branch toward the normal branch vertex both the HBO rms amplitude and the time lags decreased. The data in regions 5–8 in the middle of the horizontal branch are relatively sparse. This led to large errors bars in the time delay spectra of these regions. The 10 measured time-delay spectra of the HBO first harmonic, and the four measured time-delay spectra of the second harmonic for regions 1–4, are shown in Figure 3. In addition, we measured a composite, best-fit *phase*-delay spectrum for the low-intensity end of the horizontal branch by averaging all cross amplitudes within one FWHM of the HBO peak for intensity regions 1–3. Because the HBO

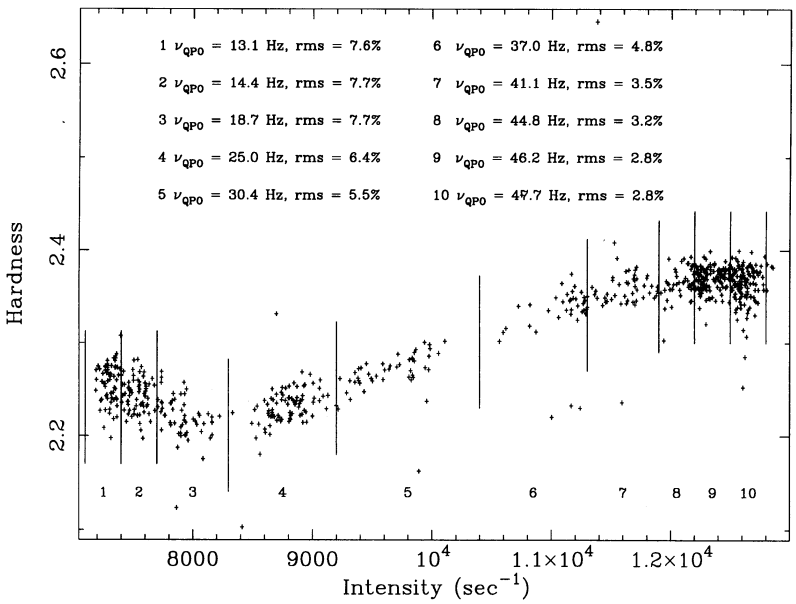

FIG. 1.—Spectral hardness (the ratio of 5.8–18.4 to 1.2–5.8 keV flux) vs. source intensity of GX 5−1 on the horizontal branch. Numbers at the bottom indicate region numbers, as used in the text.

frequency varies with intensity, different frequency ranges are averaged for each region. For this reason we quota phase rather than time delays for the composite. We did the same for the second harmonic. The phase delay spectra are shown in Figure 4.

The time-delay spectra vary with source intensity, but exhibit certain common characteristics. The time delay is an increasing function of energy. There is evidence for a leveling off at 10–12 keV in the time-delay spectra of regions 1–5 independent of intensity, hence of HBO frequency. Limited S/N in regions 6–10 make it impossible to determine if the time-delay spectra level off, but a leveling off as in regions 1–5 is statistically consistent, at the 3 σ level, with the observed time-delay spectra. In some time-delay spectra, particularly for region 2, there is evidence for a turnover both at low and at high energies in both the HBO first and second harmonic time-delay spectra. The magnitude of the maximum time delay decreases with intensity from ~4 ms for region 1 to 1 ms for region 6. We discuss the time delay spectra in the context of Compton scattering and shot models in the following section.

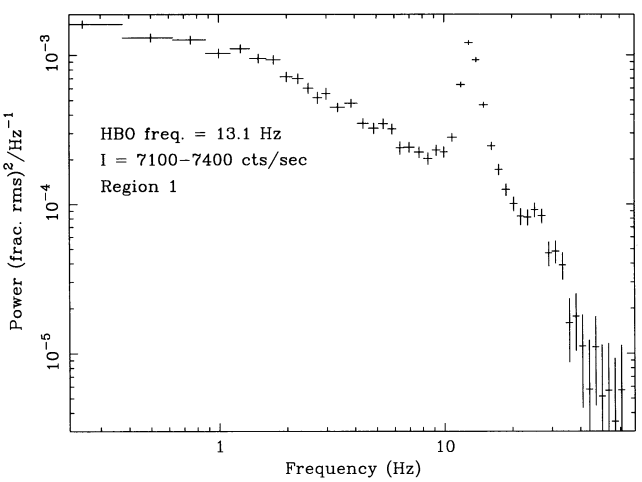

FIG. 2.—Power spectrum of GX 5−1 intensity region 1, 1.2–18.4 keV. The intensity is ~700 millicrab.

In addition to HBO time-delay spectra we binned the data into two spectral channels and measured time delays as a function of Fourier frequency from 1 to 35 Hz using a two-channel cross spectrum. Such a procedure makes it possible to investigate the intensity dependence of the time lags and facilitates comparison with previous observations. We chose 1.2–5.8 keV for the low-energy channel and 5.8–18.4 keV for the high-energy channel, both to utilize all the energy channels and to match as closely as possible the *EXOSAT* channels used in the previous analysis of time delays in GX 5−1 (van der Klis et al. 1987). The time delay is plotted in Figure 5*a* as a function of intensity. We plot the phase delay as a function of intensity in Figure 5*b*. The time delay decreases with intensity from 2.0 ± 0.2 ms at 7000 counts s^{-1}, the lowest intensity observed, to 0.16 ± 0.2 ms at 11,000 counts s^{-1}, then increases again to 0.87 ± 0.2 ms at 12,800 counts s^{-1}, at the normal-branch vertex. The phase delay decreases from 0.025 ± 0.003 at 7000 counts s^{-1} to 0.019 ± 0.003 at 10,000 counts s^{-1}, then increases to 0.041 ± 0.01 at the normal branch vertex.

4.2. *Low-Frequency Noise Phase-Delay Spectra*

We measured the energy, intensity, and Fourier frequency dependence on phase differences in the low-frequency noise, defined as 0.25 to 2 Hz. Rather than convert phase delays to time delays, we quote phase delays because there is no preferred frequency to divide by.

To investigate the energy dependence of the low-frequency noise phase lags, we determined χ^2 best-fit phase delay spectra by the same technique used to find the HBO first and second harmonic time-delay spectra. Figure 6 shows phase delay spectra of intensity regions 1, 3, and 5 obtained by averaging Fourier frequencies from 0.25 to 2 Hz. A negative phase difference indicates that the low-energy photons lag the high-energy

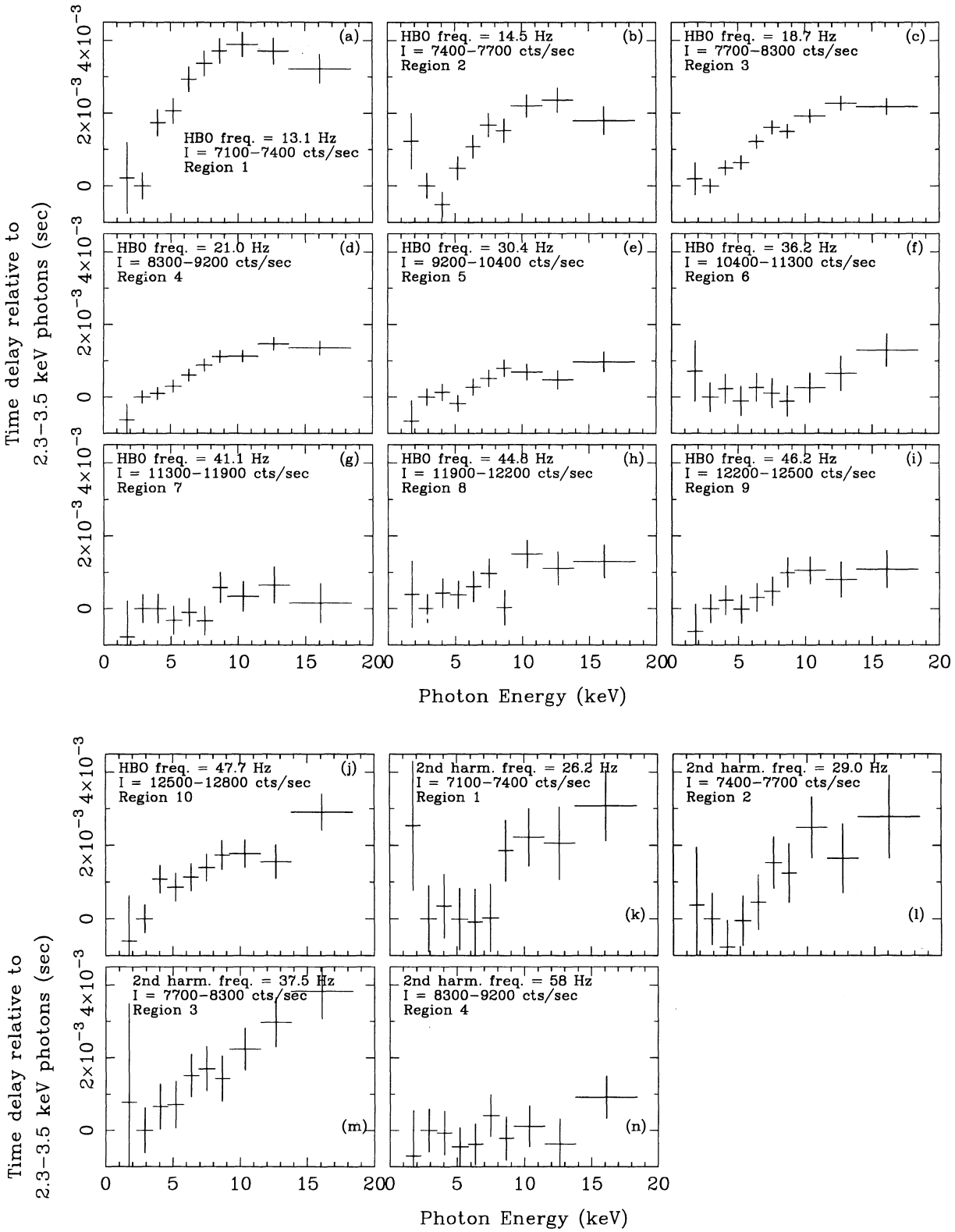

FIG. 3.—(*a–n*) First and second harmonic time-delay spectra, obtained by finding best fits to observed cross spectra. A positive value indicates a hard delay. The HBO first or second harmonic frequency is indicated in each plot.

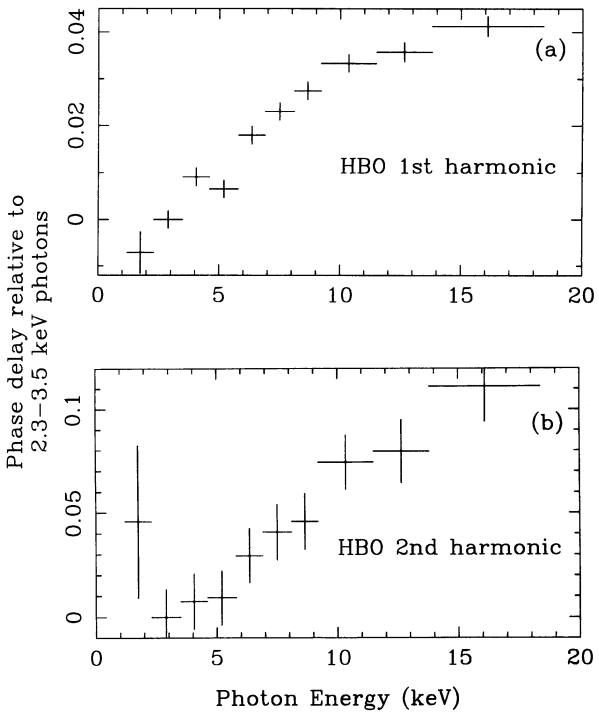

FIG. 4.—(*a–b*) Phase delay spectra of the HBO first and second harmonics, obtained by averaging measured cross amplitudes within one FWHM of the HBO first or second harmonic peak for intensity regions 1–3.

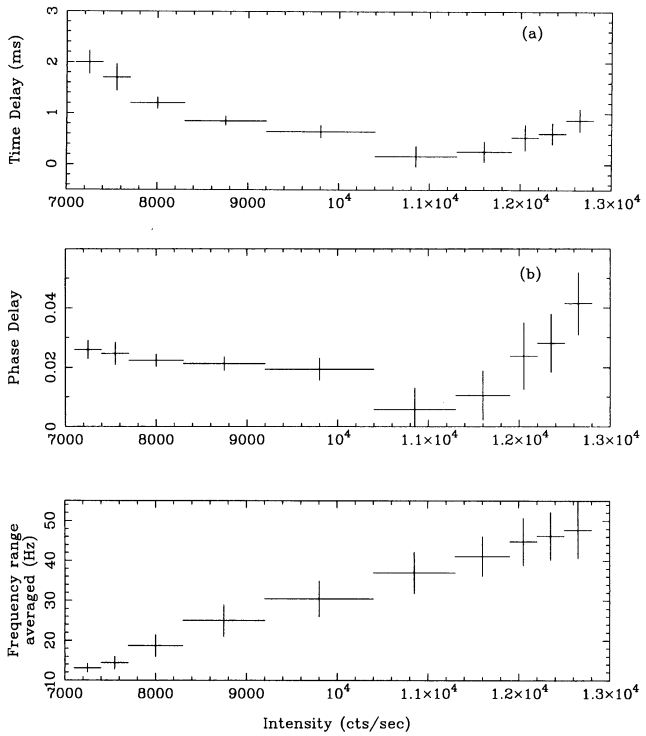

FIG. 5.—(*a*) Intensity dependence of the time delay between variations in 5.8–18.4 keV relative to those in 1.2–5.8 keV at the HBO frequency. (*b*) Phase delays, same energy ranges. The phase delay is ν times the time delay and thus contains the same information. A positive delay indicates a hard lag.

photons. We find that variations in low-energy photon intensity lag behind variations in high-energy photon intensity. The length of the low-energy lag increases with energy up to a maximum of ~ 0.03. At 1 Hz, a phase difference of 0.03 translates to a time difference of 30 ms. The magnitudes of the low-frequency noise phase lags are comparable to the magnitudes of the HBO phase lags, but with opposite sign. Because the Fourier frequency is much lower, the length of the low-frequency noise time lags is an order of magnitude greater than the length of the HBO time lags.

The phase delay spectra of regions 1, 3, and 5 are qualitatively similar. To investigate the intensity dependence, we binned the data into two spectral channels, as in the previous subsection, and measured the phase delay as a function of source intensity for the frequency range 0.25–2 Hz. The result is shown in Figure 7. Notice that the phase delay decreases with source intensity. The average phase delay in the intensity range 10,000–12,800 counts s^{-1} is 0.013 ± 0.003.

To measure the Fourier frequency dependence of the phase delays, we again chose the same two broad spectral channels and calculated the cross spectrum. Results for intensity regions 1, 3, and 5 are shown in Figures 8*a*–8*c*. It is difficult to determine if the phase delay varies with Fourier frequency at low frequency because of the large uncertainties in the phase lags. To improve the statistics, we combine intensity regions 1–5 and calculated a composite cross spectrum. The result is shown in Figure 8*d*. We find that the low-energy phase delay decreases with Fourier frequency. Because the time delay is equal to the phase delay divided by the Fourier frequency, the time delay decreases even more rapidly with Fourier frequency.

4.3. *Coherence Spectra*

Using the best-fit Fourier coefficients determined with the χ^2 technique we computed coherence spectra (cf. § 3.2) of the

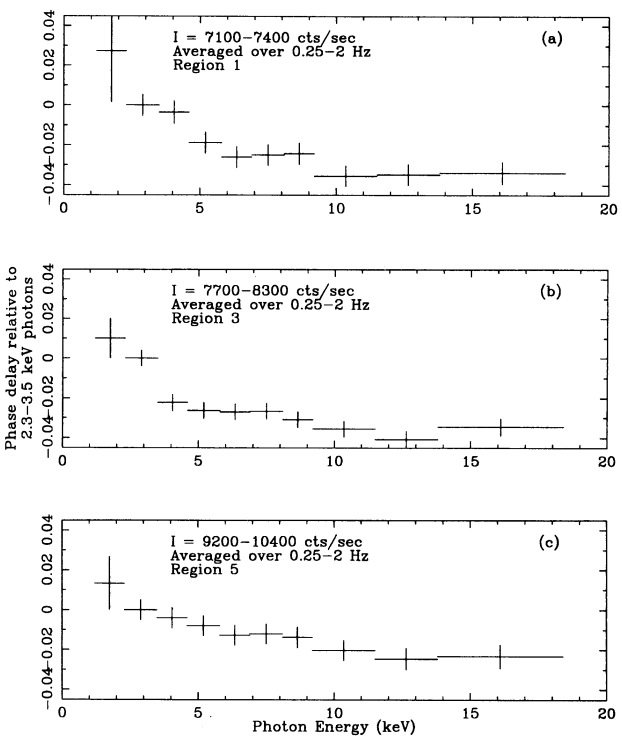

FIG. 6.—(*a–c*) Phase delay between hard and soft intensity variations in the low-frequency noise, 0.25–2 Hz, for intensity regions 1, 3, and 5. A negative value indicates a soft lag. In all cases the soft photons lag the hard photons, and in all cases the length of the lag increases with hard photon energy. For a Fourier frequency of 1 Hz, a phase delay of 0.015 corresponds to a time delay of 15 ms.

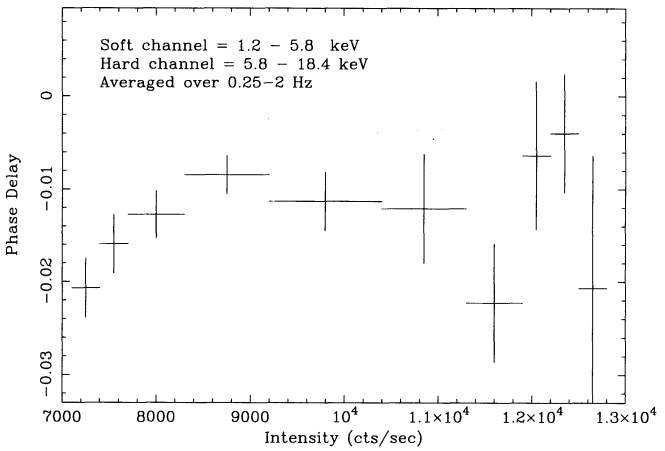

FIG. 7.—Phase delay between hard and soft photon intensity variations in the low-frequency noise as a function os source intensity. The soft channel is 1.2–5.8 keV, as the hard channel is 5.8–18.4 keV. A negative value indicates a soft lag. Frequencies from 0.25–2 Hz averaged.

HBO in intensity regions 1 and 3. The coherence spectra, corrected for Poisson noise and thus measuring intrinsic coherence, are shown in Figure 9. We found that for all spectral channels the coherence is consistent with unity. As explained in § 3.2, a value of unity is consistent with the reduced χ^2 values obtained in the fits. Reduced χ^2 values for the best-fit time-delay spectra are consistent with unity at the 3 σ level for all intensity regions.

The measured intrinsic coherence spectrum tells us that within the errors, the HBO signal in each spectral channel is the same up to a phase and amplitude factor, suggesting that the same physical mechanism is responsible for all the signals. There is no measurable source of intrinsic variability in the HBO frequency range in any spectral channel that is uncorrelated with the other spectral channels. We can typically exclude such independent variability at a level of 20% of the HBO rms variability.

Because the coherence spectrum of the GX 5−1 HBO is unity, the correlated power is equal to the total intrinsic (Poisson-noise-subtracted) power in the HBO frequency range. If the same is true at all frequencies, the correlated power as a function of Fourier frequency in each spectral channel will be the same as the power spectrum, with Poisson noise subtracted, in that channel. In that case it is possible to estimate the power spectrum of the source using only cross spectra. Cross spectra have the advantage that they are sensitive only to correlated power, and hence have no Poisson noise offset. Cross spectra can be used to estimate intrinsic power spectra without requiring the estimate of the Poisson noise level. Perfect coherence also means that if one divides the data into two broad spectral channels and calculates the amplitude of

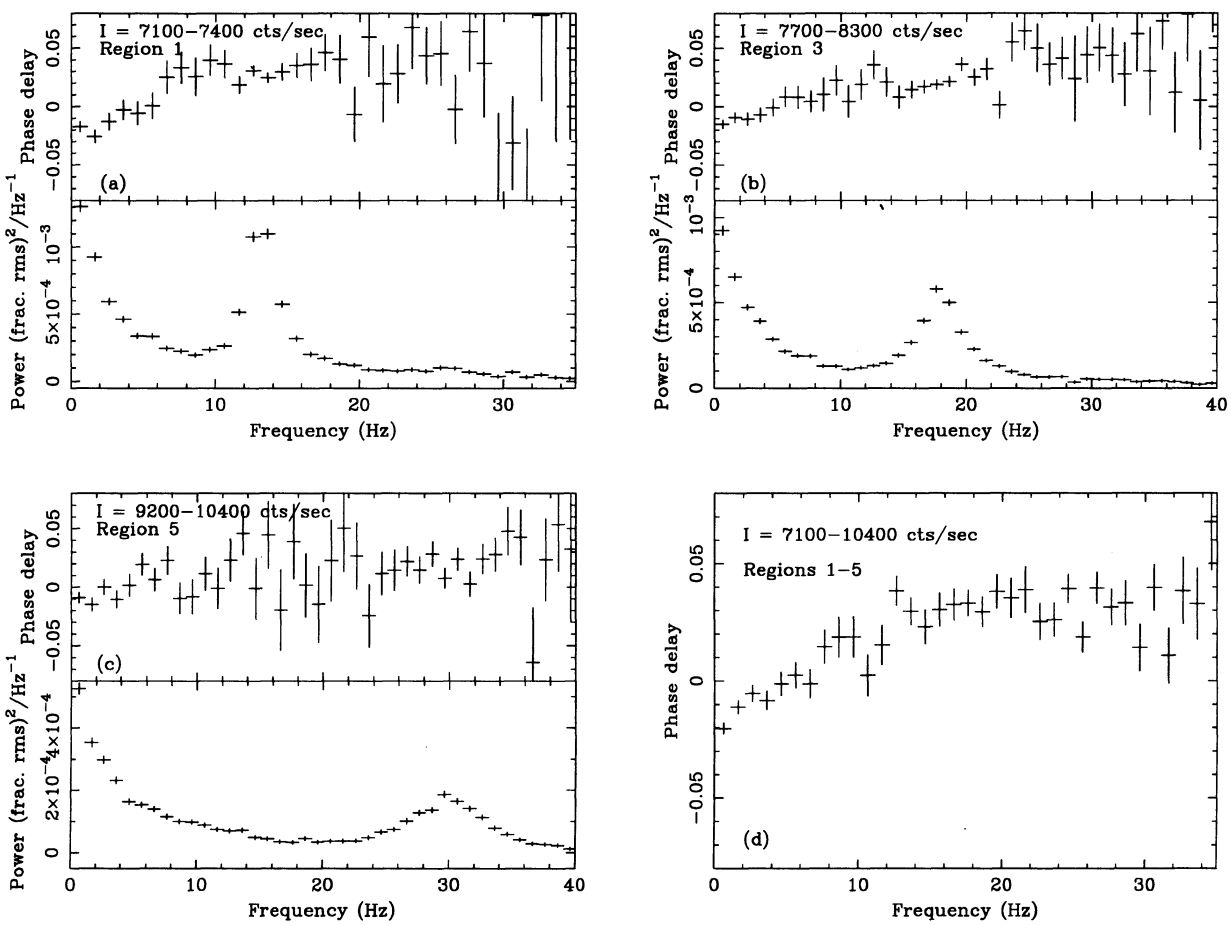

FIG. 8.—(*a–c*) The phase delay between hard and soft photons as a function of Fourier frequency. Energy channels same as Fig. 5 and 7. A negative value indicates a soft lag. Panel *d* was obtained by averaging over intensity regions 1–5.

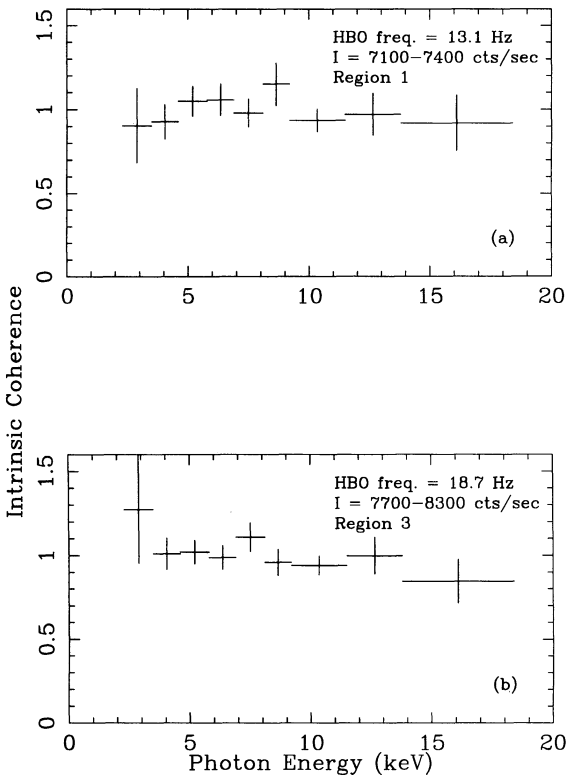

FIG. 9.—(*a–b*) Cross spectral coherence at the HBO frequency for intensity regions 1 and 3 as a function of energy. By definition, a value of unity implies a perfect correlation between intensity variations of a channel and variations in the other channels. The coherence values plotted here have been corrected for the effect of Poisson noise and hence represent measurements of intrinsic source coherence.

the cross spectrum between the two channels as a function of Fourier frequency, the resulting amplitude cross spectrum will be nearly, although not necessarily exactly, the same as the shape of the intrinsic power spectrum of the sum of all of the spectral channels. The amplitude cross spectrum is a quick method of determining the shape of the power spectrum, requiring no Poisson noise subtraction. Figure 10 shows the amplitude of the cross spectrum between spectral channels 1–4 (1.2–5.8 keV) and channels 5–10 (5.8–18.4 keV) in intensity region 1 as a function of Fourier frequency. The HBO first harmonic peak is clearly visible. The second harmonic peak is perhaps visible as a broad shoulder. Compare Figure 10 with Figure 2.

5. DISCUSSION

5.1. *Compton Scattering Model*

To investigate the possibility that the time delays we observed are caused by inverse Compton scattering we performed Monte Carlo simulations of scattering in a finite, homogeneous, spherical Comptonizing cloud centered on the neutron star. We attempted to synthesize both the energy spectrum and the time-delay spectrum. The input spectrum is a blackbody. The principal physical parameters of the model are the blackbody temperature of the input spectrum, the electron temperature and optical depth of the Comptonizing cloud, and the cloud radius. The cloud radius affects only a time-delay spectrum, and only by a scaling factor. For a detailed discussion of numerical calculations of Comptonization in a

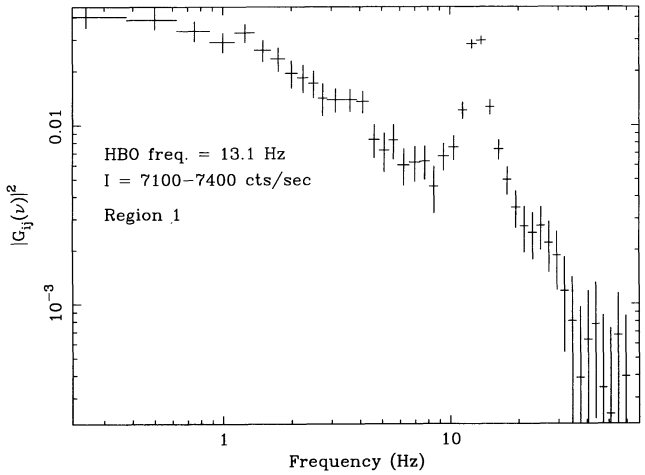

FIG. 10.—The amplitude of the cross spectrum between the 1.2–5.8 keV and 5.8–18.4 keV light curves for intensity region 1. Compare this with Fig. 2. Because this figure was obtained using cross spectra that are only sensitive to correlated variability, there is no noise offset, and no Poisson subtraction was necessary to obtain this figure.

cloud, see Pozdnyakov et al. (1983). The code we used was developed by Wijers, an Paradijs, & Lewin (1987). Recently, Schulz & Wijers (1993) used the code to fit the energy spectra of a number of low-mass X-ray binaries, including GX 5−1, all along their horizontal, normal, and flaring branches.

In Figure 11 we show a time-delay spectrum obtained with the Comptonization model using a 0.7 keV blackbody input spectrum and a 6 keV Comptonizing cloud with an optical depth of 5.6 and a radius of 5×10^7 cm. The blackbody temperature, electron temperature, and optical depth are best fit GX 5−1 values from Schulz & Wijers (1993) for the low-intensity end of the horizontal branch. By increasing the blackbody temperature and decreasing the Compton temperature we can obtain time-delay spectra with turnovers at both low and high energy, but at the expense of the worse fit to the energy spectra. This simple scattering model can reproduce the main features of the time delay and energy spectra.

There are problems, however, with the Comptonization

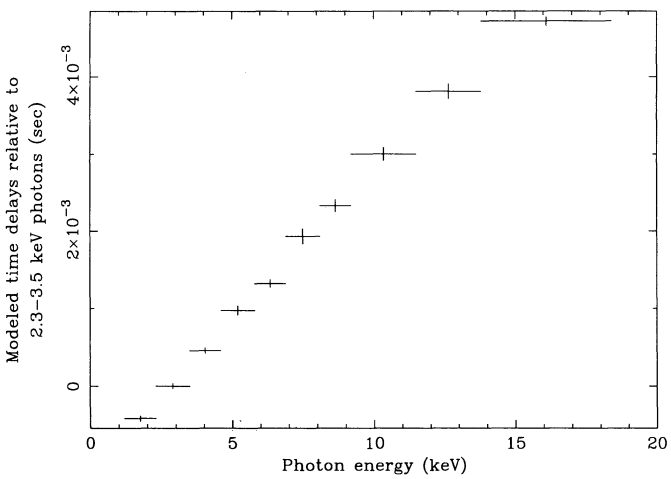

FIG. 11.—Time-delay spectrum obtained using a Monte Carlo simulation of photon scattering in a spherical, isothermal, homogeneous central corona. The blackbody temperature is 0.7 keV. The cloud has a Compton temperature of 6 keV, an optical of 5.6, and a radius of 5×10^7 cm.

model. The code used in our simulations assumes the existence of an isothermal and homogeneous cloud around the neutron star. It does not attempt to be self-consistent. Estimates of the energy-loss rate to photons traversing an electron cloud with an optical depth of order unity and with a large enough radius ($\sim$1000 km) and temperature ($\sim$10 keV) to produce 3 ms time delays indicate that neither conversion of gravitational energy nor radiative heating can provide enough energy to the cloud at large radii to maintain the cloud temperature (Stollman et al. 1987; Shibazaki et al. 1988). Thus, the model has problems with energy conservation.

Observationally, there are two difficulties. The comptonization model predicts that signals in different channels are copies of one another, up to a shift in time and a scaling in amplitude, as long as the time scale of variations in the signals is much longer than the time delays between the signals. The signal we observe in each spectral channel at the HBO time scale should be modulated with the same relative amplitude as the input signal that produced it, delayed by up to several milliseconds. Therefore the HBO rms amplitude spectrum—fractional rms amplitude as a function of energy—should be flat. Further, the time delay between any two channels should be independent of Fourier frequency, provided the Fourier period is much longer than the time-delay.

The observed fractional rms amplitude spectrum is shown in Figure 12. All values have been corrected for cross talk induced by dead time using the frequency domain technique described in Lewin et al. (1992) and, independently, using a time domain technique as described in Mitsuda & Dotani (1989), with consistent results. Note that the assumption made by Lewin et al. in calculating rms amplitudes of HBO in GX 5−1 for this same data set—that the magnitudes of horizontal-branch time delays are small enough relative to the HBO frequency that the time delays may be neglected in computing dead-time–induced corrections to the rms amplitudes—is correct. We see that the fractional rms amplitude is much larger at high energies than at low. Thus, a simple Compton model as presented here is inconsistent with the fractional HBO rms amplitude spectrum observed.

A second difficulty with the Comptonization model arises from the time delay spectrum of the HBO second harmonic. Recall that the measured time delay at frequency ν is defined as the phase difference at frequency ν divided by ν. The phase-delay spectrum of a set of signals in a frequency range centered at ν_0 is identical to the time-delay spectrum, with a multiplicative factor of ν_0. A phase-delay spectrum is an alternate way of presenting a time-delay spectrum. If the observed delays are true time delays, as will be the case if Comptonization is responsible for the delays, the prediction is that the first and second harmonic will show an identical time-delay spectrum, or in other words the phase delay of the second harmonic will always be twice that of the first harmonic. The ratio of the phase delay spectrum of the second harmonic to the phase-delay spectrum of the first harmonic, the ratio spectrum, should be flat, and should have a value of 2. We calculated the ratio spectrum using values found by the χ^2 technique to evaluate the hypothesis of an identical time delay.

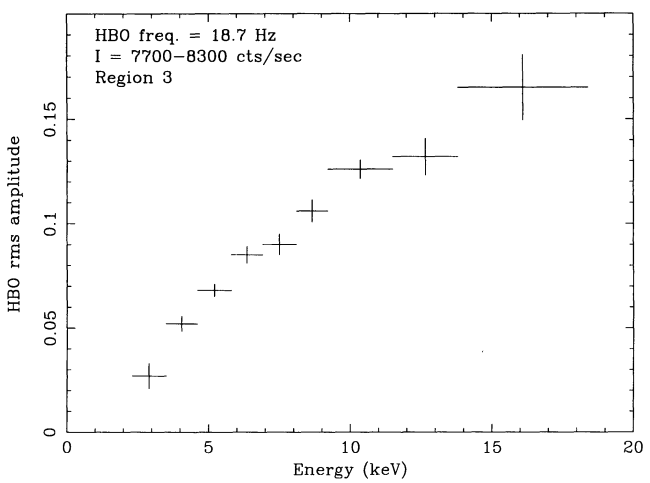

FIG. 12.—HBO fractional rms amplitude as a function of energy for the HBO in intensity region 3. The fractional rms amplitude increase with energy from $\sim$6% in the range 1.2–2.3 keV to nearly 20% in the range 13.8–18.4 keV.

In Figure 13 we show the ratios of the second to the first harmonic phase delay spectra (ratio spectra) for regions 1–3. Figure 13*d* is the ratio of the average HBO second harmonic phase delay spectrum, combining data in regions 1–3, to the average HBO first harmonic phase delay spectrum of those regions, i.e., the ratio of Figure 4*b* to Figure 4*a*. To obtain the average phase delay spectra combining regions 1–3 we used data within one FWHM of the HBO first and second harmonic peaks in each intensity region. Thus, the Fourier frequency range over which the average is performed is different for the four different intensity regions. For this reason we use the ratio of phase delay spectra, rather than time-delay spectra.

Notice that in each region the ratio spectrum increases with energy. The increase is even more apparent in the average ratio spectrum. A nonconstant ratio spectrum contradicts the Compton model prediction. We can either conclude that the model is wrong, or that another signal, with a different time-delay spectrum, is influencing our results.

We can estimate the possible effect of the low-frequency noise contribution because we know how its amplitude depends upon frequency. At the HBO first and second harmonic frequencies, we find that its Fourier amplitude is so small that it will not have a measurable effect upon the HBO time-delay spectra, regardless of the phases of the low-frequency noise Fourier coefficients.

Another possibility is that there is a high-frequency noise signal with a different phase-delay spectrum that has different effects upon the first and second harmonic phase delay spectra. Because of the low Nyquist frequency of the data used (64 Hz) we could not evaluate the strength of the high-frequency noise. Previous observations at higher time resolution have found high-frequency noise components with fractional rms amplitude variations of order a few percent (Hasinger & van der Klis 1989). We cannot rule out the possibility that such a signal is causing the differences between the first and second harmonic phase delay spectra.

Finally, the Compton model predicts a flat ratio spectrum only if all the radiation originates at or extremely near the neutron star surface. If the disk also emits, its radiation would be softer. The increase in the ratio spectrum with energy may reflect that at higher energies a higher fraction of the radiation comes from Compton reprocessing of photons from the neutron star surface. However, for disk radiation to contribute to either the HBO first or the second harmonic time-delay spectrum, its intensity must be modulated at the HBO first or second harmonic frequency.

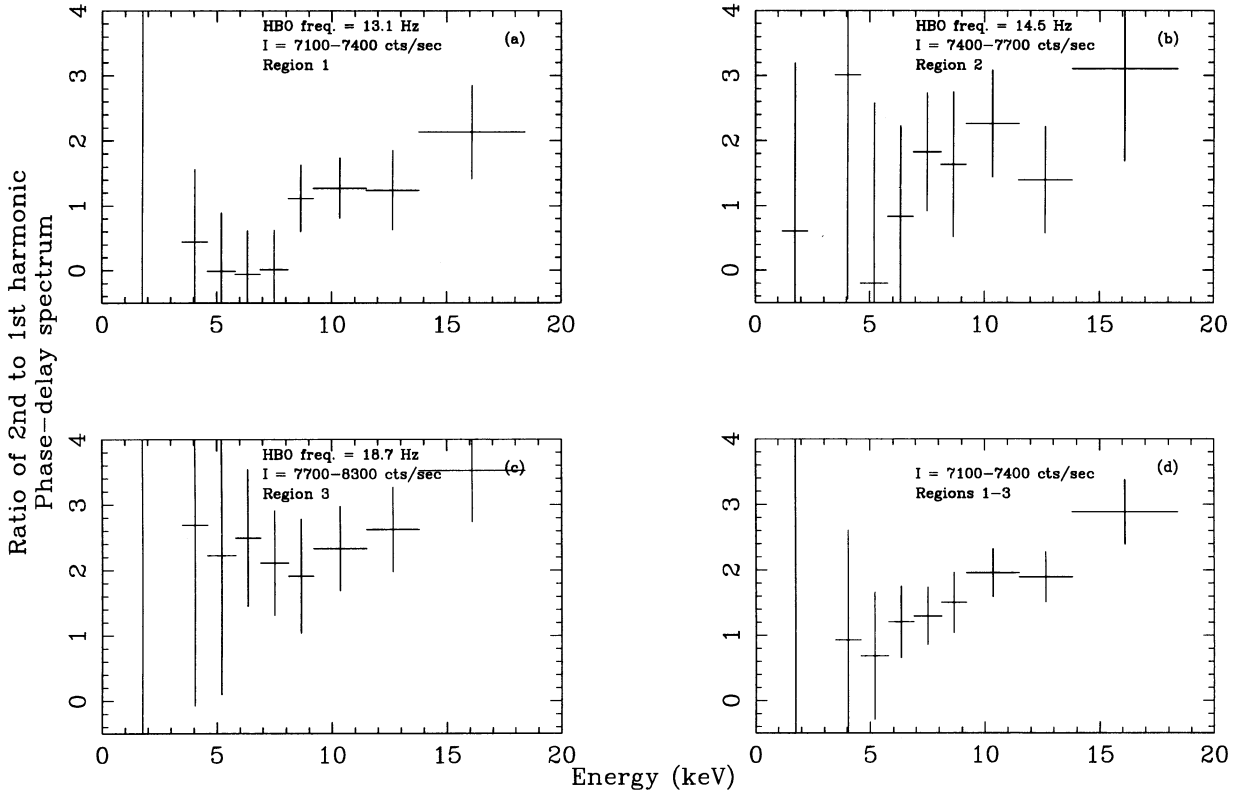

FIG. 13.—Ratio of the HBO second to the first harmonic phase delay spectrum for intensity regions 1–3. (*a–c*) In all cases the ratio increases with hard photon energy, in contrast to the prediction of the Comptonization model. (*d*) The ratio of the second to the first harmonic phase-delay spectrum for an average of intensity regions 1–3.

5.2. *Evolving Shot Models*

The intensity modulations causing HBO peaks in power spectra of low-mass X-ray binaries are thought to originate near or at the neutron star surface as material falls through the magnetosphere and onto the surface of the neutron star. Shot noise models are the mathematical class of models that describe variations in intensity as a stochastic series of overlapping shots. They have been invoked to explain the X-ray light curves and power spectra of low-mass X-ray binaries. See Alpar & Shaham (1985) for a description of shot models.

It is possible that the observed low-energy lags at low Fourier frequencies occur because the shot envelopes in the lower energy channels lag and/or differ from those in the higher energy channels (van der Klis et al. 1987; Shibazaki et al. 1988). Such a model comes under the general heading of a softening shot model. Shibazaki et al. (1988) discuss softening shots in detail in the context of standard QPO shot models, such as the beat frequency modulated accretion model (Alpar & Shaham 1985; Lamb et al. 1985; Shibazaki & Lamb 1987). They find that energy-dependent shot profiles can produce low-energy phase lags in the cross spectrum at frequencies typical of the shot time scale (tenths of a Hertz to a few Hertz) without noticeably affecting the cross spectrum at higher frequencies.

To simultaneously explain the low Fourier frequency low-energy phase lags and the higher frequency high-energy phase lags, the shot envelopes causing the low-frequency noise must be treated independently of the oscillations in the shots causing the HBO peak. The high-energy lag in the HBO can be explained if the oscillations causing the HBO peak in the higher energy channels lag those in the lower energy channels. If an energy-dependent response function, $h(E, \Delta t)$, connects the accretion rate, $r(t)$, across an accretion gap onto the neutron star, with the observed intensity at energy E and time $t + \Delta t$, the observed time delays will reflect differences in the characteristic conversion time as a function of energy. However, if the response function is the mathematical realization of heating as blobs fall to the surface, the delays should be of order the free-fall time. Since the free-fall time is no more than 0.5 ms, 4 ms delays should not be produced. Mathematically, shot models can produce almost any time-delay spectrum, but like Comptonization models, they have problems on physical grounds.

5.3. *Time Delays and Millisecond Pulsar Searches*

If the HBO time-delay spectrum is caused by an external process that acts upon signals produced in the inner disk or at the neutron star, rather than being intrinsic to to the HBO signal itself, we may think of the process as a kind of dispersion that will act upon any signal produced at or near the neutron star, regardless of its frequency. One particularly interesting kind of signal originating at the neutron star surface is coherent pulsations. Making no assumptions about the physical nature of the process causing the time delays—only that it is dispersive—we can calculate its effect upon the sensitivity of millisecond pulsar searches.

Millisecond X-ray pulsar searches have been conducted using X-ray data with the high time resolution available, which for current instruments is typically of order 1 ms (Wood et al. 1991). Millisecond data always have a smaller number of wide

energy channels, as high time resolution necessarily comes at the expense of spectral resolution due to satellite telemetry limitations. For spectral channels typical of *Ginga* or *EXOSAT* and for a time-delay spectrum such as we see in GX 5−1, the signal at the low end of a spectral channel can arrive milliseconds earlier than the signal at the high end. In Cyg X-2, horizontal branch time lags observed with *EXOSAT* are even larger (van der Klis et al. 1987). We calculate how much the observed power from a coherent oscillation is reduced by such time delays.

Assume a signal $x(t)$ is produced at the neutron star surface. An unspecified process acts upon the input signal with the result that in a narrow spectral channel of energy E and width dE we observe $y(t) = A(E)x[t - r(E)]dE$. In a broader spectral channel extending from $E = E_-$ to $E = E_+$ we observe

$$y(t) = \int_{E_-}^{E_+} A(E)x[t - \tau(E)]dE \, . \tag{14}$$

To calculate the loss of sensitivity as a function of the signal frequency ν_0 caused by a time-delay spectrum $\tau(E)$ we calculate the power spectrum and compare the power at ν_0 with the power we could observe for $\tau(E) \equiv 0$.

The Fourier transform $Y(\nu)$ of $y(t)$ is given by

$$Y(\nu) = \int_0^T y(t)e^{2\pi i\nu t} dt \, . \tag{15}$$

Substituting equation (14) for $y(t)$ and integrating over time yields

$$Y(\nu) = X(\nu) \int_{E_-}^{E_+} A(E)e^{2\pi i\nu\tau(E)} dE \, , \tag{16}$$

where $X(\nu)$ is the Fourier transform of $x(t)$. Ignoring normalization, the power at the signal frequency becomes

$$P(\nu_0) = |X(\nu_0)|^2 \left| \int_{E_-}^{E_+} A(E)e^{2\pi i\nu_0\tau(E)} dE \right|^2 . \tag{17}$$

For $\tau(E) \equiv 0$, the power is

$$P(\nu_0) = |X(\nu_0)|^2 \left[\int_{E_-}^{E_+} A(E)dE \right]^2 . \tag{18}$$

The fractional power in the presence of time delays is given by the ratio of equation (17) to equation (18). One minus this ratio gives us the fractional loss of power. Thus, we define

$$F_{\rm loss}[\nu_0, A(E), \tau(E)] = 1 - \frac{|\int_{E_-}^{E_+} A(E)e^{2\pi i\nu\tau(E)}dE|^2}{[\int_{E_-}^{E_+} A(E)\,dE]^2} . \tag{19}$$

In Table 1 we tabulate $F_{\rm loss}[\nu_0, A(E), \tau(E)]$ in regions 1, 3, and 10 of the hardness-intensity diagram for pulsar frequencies of 50, 100, and 500 Hertz. To calculate $F_{\rm loss}$ it is always necessary to specify pulsed rms amplitude as a function of energy and a response matrix for the instrument observing the pulsar. The values tabulated below were calculated using the observed *Ginga* PHA spectra of GX 5−1 and assuming the fractional rms amplitude spectra of pulsars are flat. It is important to note that the calculated losses are thus specific to the instrument and to the source.

TABLE 1

PULSAR SEARCH FRACTIONAL POWER LOSS DUE TO ENERGY-DEPENDENT TIME DELAYS IN A BROAD SPECTRAL CHANNEL

Region	$F_{\rm loss}$ (50 Hz)	$F_{\rm loss}$ (100 Hz)	$F_{\rm loss}$ (500 Hz)
1	0.020 ± 0.005	0.080 ± 0.020	0.91 ± 0.05
3	0.003 ± 0.001	0.011 ± 0.005	0.25 ± 0.10
10	0.004 ± 0.002	0.016 ± 0.007	0.34 ± 0.11

NOTES.—The spectral channel extends from 1.6–6 keV. The pulsed component is assumed to have a flat rms amplitude spectrum and a typical low-mass X-ray binary PHA spectrum. If the pulsed component has a narrow energy spectrum, the losses will be smaller.

To perform the integral in equation (19) we fitted the observed PHA spectrum in the range 1.2–5.8 keV using a parabola and fitted the time-delay spectra in the same energy range with a straight line. Because an offset of the line fit to the time-delay spectra will not affect $F_{\rm loss}$, only a single parameter—the slope—is important. To determine uncertainties, we treated the fit to the PHA spectra as fixed and used the uncertainties in the slopes of the time-delay spectra to determine 1 σ confidence intervals. The spectral range of the detector is taken to be 1.6–6 keV, a range typical for both *Ginga* and *EXOSAT*.

In region 3 where the time delays are small, the loss of power is less than 1% for pulsar frequencies under 100 Hz and reaches only ~25% at 500 Hz. The losses are smaller in intensity regions 4–8, and comparable in regions 9 and 10. Millisecond pulsar searches, already hampered by small expected signal modulation depths due to weak low-mass X-ray binary magnetic fields and possible losses from gravitational lensing (Wood, Ftaclas, & Kearney 1988; Mészaros, Riffert, & Berthiaume 1988; Wood et al. 1991 and references therein), may thus be relatively free of dispersive losses on a large fraction of the horizontal branch. However, if the dispersion is caused by cloud scattering, the isotropizing effect of the cloud may be much worse (Brainerd & Lamb 1987; Wang & Schlickeiser 1987; Bussard et al. 1988). The case calculated here considers only the effect of time differences, independent of the direction in which the photon escapes. In intensity regions 1 and 2, the larger time delays produce losses of up to 90% at high frequency. As a rule, if the change in time delay over a spectral channel is large relative to the Fourier period, a significant loss in power will result.

We would like to thank J. Norris for helpful discussion. W. H. G. L. gratefully acknowledges support from the National Aeronautics and Space Administration under grant NAG 8-700. R. W. is supported by a Compton Fellowship (grant NAG 5-1816) and acknowledges travel support from the LKBF. J. v. P. acknowledges support from NATO through grant RG 331/88. This work was supported in part by the Netherlands Organization for Scientific Research (NWO) under grant PGS 78-277.

APPENDIX

χ^2 TECHNIQUE

In the text we describe the procedure for finding best-fit time delay spectra as a χ^2 minimization search for best-fit Fourier coefficients whose phases give us the time delays. It is not, however, the absolute phases of the Fourier coefficients that we expect to be constant from one independent data segment to the next but their relative phases. Under the assumption that the relative phases of the Fourier coefficients at a given Fourier frequency are the same from segment to segment we can write the Fourier coefficient of channel m in segment p at frequency ν_j as

$$Y_{mp}(\nu_j) = H_m(\nu_j)X_p(\nu_j) , \tag{20}$$

where $H_m(\nu_j)$ is constant from segment to segment and $X_p(\nu_j)$ is a complex number whose phase is drawn from a distribution uniformly and randomly distributed on $[0, 2\pi]$. $H_m(\nu)$ is the frequency response function, or frequency domain transfer function. Averaging over the Fourier frequency range of interest and assuming that the phase delay is approximately constant yields

$$Y_{mp} = H_m X_p . \tag{21}$$

Next compute the cross spectrum is segment p:

$$G_{mn,p} = Y^*_{mp} Y_{np} = H^*_m H_n |X_p|^2 . \tag{22}$$

Averaging over a large number of segments yields

$$G_{mn} = H^*_m H_n \langle |X|^2 \rangle . \tag{23}$$

In deriving equations (23) we have assumed only that the phase differences between the spectral channels are constant between segments. To give a physical interpretation of the above equations, assume that equations (20) holds at all frequencies. By taking the inverse Fourier transform of equations (20) we get the convolution integral

$$y_m(t) = \int_{-\infty}^{\infty} h_m(\tau)x(t - \tau)d\tau , \tag{24}$$

where $y_m(t)$ is the right curve in channel m and $h_m(\tau)$ is the transfer function or unit impulse response function, so called because a unit area δ function input, $x(t) = \delta(t)$, produces output $y_m(t) = h_m(t)$. The signal $x(t)$ is an input that is convolved with each of the transfer functions $h_m(\tau)$ to produce the observed output signals $\{y_m(t)\}$. The input $x(t)$ is generally not observable. We only see the $y_m(t)$. Note that the input signal is a mathematical convenience. There need be no actual input signal for the χ^2 procedure to work. The real physical assumption is that the relative phases of the HBO signals are constant. The coherence function defined below and in § 3 is a quantitative measure of the validity of this assumption, as is the χ^2 value of the best fit. Even if the relative phases are not constant the best-fit time-delay spectrum is an estimate of the average relative phases, hence of the time-delay spectrum. A system described by equations (24), or equivalently by equations (20) is called a constant parameter linear system if the transfer functions do not change with time.

Good discussions of linear systems theory can be found in books on signal processing. See, for example, Bendat & Piersol (1980, 1986). Much of the background material presented here and in § 3 is covered in detail in chapters 6 and 9 of Bendat & Piersol (1986).

We use equation (23) as the basis of the χ^2 technique. The quantities we wish to find using χ^2 minimization are the transfer functions H_m. The average Fourier amplitude of the input signal is $\langle |X|^2 \rangle$. By assumption we cannot observe the input so $\langle |X|^2 \rangle$ cannot be measured, but it is the same for each m, n pair, so we do not need it to estimate the relative amplitudes of the transfer functions. Further, equation (23) are invariant under a transformation of the form $H_m \rightarrow e^{i\phi}H_m$. We thus cannot determine the absolute phases of the transfer functions, only their relative phases, a result of our ignorance of the absolute phase of the input signal.

Setting $\langle |X|^2 \rangle = 1$ yields the set of equations

$$G_{mn} = H^*_m H_n . \tag{25}$$

From the set of equation (25) we define the χ^2 static

$$\chi^2 = \sum_{m<n} \frac{|\hat{G}_{mn} - H^{\rm fit*}_m H^{\rm fit}_n|^2}{\sigma^2_{mn}} \tag{26}$$

where we show how to estimate σ_{mn} in the following section.

The prescription for obtaining a χ^2 best-fit time-delay spectrum for multichannel data is then as follows.

1. For each data segment measure cross- and auto-spectral densities between all pairs of spectral channels. Correct for dead-time–induced channel cross talk using either a time domain procedure as discussed in Mitsuda & Dotani (1989), or a frequency domain procedure (Lewin, van Paradijs, & van der Klis 1988). Average the cross and auto spectra over data segments.
2. Average each measured cross and auto spectrum over the Fourier frequency range of interest to obtain $\hat{G}_{mn}$ for all $m \leq n$.
3. Compute and minimize χ^2 as defined in equation (26) to find best-fit transfer functions and confidence intervals. It is crucial before minimizing to impose one additional constraint on the system. We fix the value of the real or imaginary part of one parameter. The relative amplitudes and phases of the best-fit transfer functions and thus the time delay and coherence spectra are

invariant to the choice of channel. Failure to impose an additional constraint will almost certainly cause any minimization routine to fail, and at any rate will produce meaningless confidence limits for the transfer function values. The time delay between channels m and n is given by $\arg [H_m^* H_n]/\nu$, where ν is the average Fourier frequency.

4. As always in χ^2 minimization, check that the final reduced χ^2 value is reasonable. A large value means the assumed constancy of the relative phases and amplitudes of the transfer functions from segment to segment is invalid. Either the process under investigation is nonstationary or there is an additional process at work in some or all of the channels that is uncorrelated with the process in the other channels. It does not, however, mean that the best-fit values should be rejected. Even for large χ^2, the transfer functions are a best-fit average. A truly large χ^2 value may indicate corrupted data. A single large, previously unnoticed data spike caused our χ^2 values to be enormous, although it hardly affected the best fit values of the parameters.

A2. UNCERTAINTY ESTIMATION

In this section we will remove the fit superscript from the transfer functions H_m to simplify notation. We wish to show that the χ^2 statistic to be minimized in finding best-fit values of the transfer functions can be written

$$\chi^2 = \sum_{m<n} \frac{|H_m^* H_n - \hat{G}_{mn}|^2}{\sigma_{mn}^2}, \tag{27}$$

where $\sigma_{mn}^2 = (1/2n_d)\hat{G}_{mm}\hat{G}_{nn}$. Recall that a hat indicates a quantity obtained by averaging over independent data segments and/or Fourier frequencies and that a tild indicates a "raw," or unaveraged quantity.

The usual form of the χ^2 statistic is

$$\chi^2 = \sum_{i=1}^{N} \frac{[y_i - f(x_i)]^2}{\sigma_i^2}, \tag{28}$$

where the fit function f is a function of the independent variable x and some number of fit parameters, and the values of the dependent variable y_i are the results of measurements at discrete values x_i of the independent variable. The denominator, σ_i^2, is the expected experimental variance in the observed value y_i. Fitting observed cross spectra with products of transfer functions differ from the standard χ^2 problem in that both the observed quantities and the fit functions are complex. However, we are free to consider the real and imaginary parts of the cross spectra and transfer functions to be the observables and the fit parameters, respectively. Let $\hat{G}_{mn} = \hat{G}_{mn}^R + i\hat{G}_{mn}^I$, where $\hat{G}_{mn}^R$ is the real and $\hat{G}_{mn}^I$ the imaginary part of $\hat{G}_{mn}$, and similarly let $H_m = H_m^R + iH_m^I$. We can now define a χ^2 statistic in terms of real quantities:

$$\chi^2 \equiv \sum_{m<n} \left\{ \left[\frac{(\hat{G}_{mn}^R - H_m^R H_n^R - H_m^I H_n^I)^2}{\sigma_{mn}^{R\,2}} \right] + \left[\frac{(\hat{G}_{mn}^I - H_m^R H_n^I + M_m^I H_n^R)^2}{\sigma_{mn}^{I\,2}} \right] \right\}. \tag{29}$$

It remains to calculate the uncertainties in $\hat{G}_{mn}^R$ and $\hat{G}_{mn}^I$.

Let us first find the variance in a single (unaveraged) measurement of the cross spectrum at a single Fourier frequency, $\hat{G}_{mn}(\nu_j)$. At the risk of confusion we drop the frequency in the following to simplify notation. Written in terms of Fourier coefficents, $\tilde{G}_{mn}$ becomes

$$\tilde{G}_{mn} = \tilde{X}_m^* \tilde{X}_n = \tilde{X}_m^R \tilde{X}_n^R + \tilde{X}_m^I \tilde{X}_n^I + i(\tilde{X}_m^R \tilde{X}_n^I + \tilde{X}_m^I \tilde{X}_n^R). \tag{30}$$

The real and imaginary parts of $\tilde{G}_{mn}$ we label $\tilde{C}_{mn}$ and $\tilde{Q}_{mn}$, respectively;

$$\tilde{C}_{mn} = \tilde{X}_m^R \tilde{X}_n^R + \tilde{X}_m^I X_n^I, \qquad \tilde{Q}_{mn} = \tilde{X}_m^R \tilde{X}_n^I + \tilde{X}_m^I \tilde{X}_n^R. \tag{31}$$

The variance in $\tilde{C}_{mn}$ is given by

$$\text{var}\,[\tilde{C}_{mn}] = \langle \tilde{C}_{mn}^2 \rangle - (\langle \tilde{C}_{mn} \rangle)^2. \tag{32}$$

The expectation value of $\tilde{C}_{mn}$ is C_{mn}. Expanding the expectation value of $(\tilde{C}_{mn})^2$ yields

$$\langle \tilde{C}_{mn}^2 \rangle = \langle (\tilde{X}_m^R)^2 (\tilde{X}_n^R)^2 + (\tilde{X}_m^I)^2 (\tilde{X}_n^I)^2 + 2\tilde{X}_m^R \tilde{X}_m^I \tilde{X}_n^R \tilde{X}_n^I \rangle. \tag{33}$$

The expectation value of the product of four Gaussian random variables is

$$\langle abcd \rangle = \langle ab \rangle \langle cd \rangle + \langle ac \rangle \langle bd \rangle + \langle ad \rangle \langle bc \rangle. \tag{34}$$

Using equation (34) we can evaluate equation (33). To do so we use the following relations (Bendat & Piersol 1986);

$$\langle \tilde{X}_m^R \tilde{X}_m^I \rangle = \langle \tilde{X}_n^R \tilde{X}_n^I \rangle = 0, \qquad \langle (\tilde{X}_m^R)^2 \rangle = \langle (\tilde{X}_m^I)^2 \rangle = (\tfrac{1}{2}) G_{mm}, \qquad \langle (\tilde{X}_n^R)^2 \rangle = \langle (\tilde{X}_n^I)^2 \rangle = (\tfrac{1}{2}) G_{nn},$$
$$\langle \tilde{X}_m^R \tilde{X}_n^R \rangle = \langle \tilde{X}_m^I \tilde{X}_n^I \rangle = (\tfrac{1}{2}) C_{mn}, \qquad \langle \tilde{X}_m^R \tilde{X}_n^I \rangle = \langle \tilde{X}_m^I \tilde{X}_n^R \rangle = (\tfrac{1}{2}) Q_{mn}. \tag{35}$$

We follow an analogous procedure to find the variance in $\tilde{Q}_{mn}$, and obtain

$$\text{var}\,[\tilde{C}_{mn}] = \tfrac{1}{2}(G_{mm} G_{nn} + C_{mn}^2 - Q_{mn}^2), \qquad \text{var}\,[\tilde{Q}_{mn}] = \tfrac{1}{2}(G_{mm} G_{nn} + Q_{mn}^2 - C_{mn}^2). \tag{36}$$

Averaging n_d-independent samples and Fourier frequency channels reduces the above variances by factor of $1/n_d$ with the result that

$$\text{var}\,[\tilde{C}_{mn}] = \frac{1}{2n_d}(G_{mm} G_{nn} + C_{mn}^2 - Q_{mn}^2), \qquad \text{var}\,[\tilde{Q}_{mn}] = \frac{1}{2n_d}(G_{mm} G_{nn} + Q_{mn}^2 - C_{mn}^2). \tag{37}$$

If the data under investigation is dominated by Poisson noise, as is the case in our data, both of the variances in equation (37) are dominated by the product of autospectral densities $G_{mm}\,G_{nn}$ because both the signal and the noise contribute to the autospectra. We thus obtain the approximate expression, valid when Poisson noise dominates the signal,

$$\text{var}\,[\hat{C}_{mn}] \approx \text{var}\,[\hat{Q}_{mn}] \approx \frac{1}{2n_d}\,G_{mm}\,G_{nn}\,. \tag{38}$$

The variances of the real and imaginary parts are approximately equal and we can write χ^2 as in equation (27).

We should note that equation (27) is approximate not only because the variances of the real and imaginary parts of $\hat{G}_{mn}$ are not exactly equal but because the expectation value of the covariance between $\hat{C}_{mn}$ and $\hat{Q}_{mn}$ is nonzero. However, because the covariance scales as $1/n_d$, it becomes vanishing small after averaging a large number of independent segments and frequency channels. Nonetheless, we performed χ^2 minimization using a statistic incorporating both the exact variances in equation (37) and the covariance. We found that in all cases the best-fit transfer functions and the uncertainties agreed with those found using equation 27 to within $\sim 1\%$. We thus conclude that the χ^2 method as outlined in this paper is a good approximation given a large data set in the presence of Poisson noise.

REFERENCES

Alpar, M. A., & Shaham, J. 1985, Nature, 316, 239
Bendat, J., & Piersol, A. 1980, Engineering Applications of Correlation and Spectral Analysis (New York: Wiley-Interscience)
———. 1986, Random Data; Analysis and Measurements Procedures (New York: Wiley-Interscience)
Brainerd, J., & Lamb, F. K. 1987, ApJ, 317, L33
Bussard, R. W., Weisskopf, M. C., Elsner, R. F., & Shibazaki, N. 1988, ApJ, 327, 284
Dotani, T. 1988, Ph.D. thesis, University of Tokyo, ISAS Res. Note 184
Elsner, R. F., Shibazaki, N., & Weisskopf, M. C. 1987, ApJ, 320, 527
Hasinger, G. 1987, in IAU Symp. No. 125, The Origin and Evolution of Neutron Stars, ed. D. J. Helfand & J. H. Huang (Dordrecht: Reidel), 333
———. 1988, Adv. Space Res., 8, 377
Hasinger, G., Langmeier, A., Pietsch, W., & Gottwald, M. 1985, IAU Circ. No. 4153
Hasinger, G., Langmeier, A., Sztajno, M., Trümper, J., Lewin, W. H. G., & White, N. 1986, Nature, 319, 469
Hasinger, G., Priedhorsky, W. C., & Middleditch, J. 1989, ApJ, 337, 843
Hasinger, G., & van der Klis, M. 1989, A&A, 225, 79
Hasinger, G., van der Klis, M., Ebisawa, K., Dotani, T., & Mitsuda, K. 1990, A&A, 235, 131
Kuulkers, E., van der Klis, M., Oosterbroek, T., Asai, K., Dotani, T., van Paradijs, J., & Lewin, W. H. G. 1993, A&A, submitted
Lamb, F. K., Shibazaki, N., Shaham, J., & Alpar, M. A. 1985, Nature, 317, 681
Lamb, F. K. 1988, Adv. Space Res., 8 (2), 421
Lewin, W. H. G., Lubin, L. M., Tan, J., van der Klis, M., van Paradijs, J., Penninx, W., Dotani, T., & Mitsuda, K. 1992, MNRAS, 256, 545
Lewin, W., van Paradijs, J., & van der Klis, M. 1988, Space Sci. Rev., 46, 273
Makino, F., and ASTRO-C Team 1987, Astrophys. Letters Comm., 25, 223
Mészáros, P., Riffert, H., & Berthiaume, G. 1988, ApJ, 235, 204
Middleditch, J., & Priedhorsky, W. 1985, IAU, Circ., No. 4060
———. 1986, ApJ, 306, 230
Mitsuda, K., & Dotani, T. 1989, PASJ, 41, 557
Mitsuda, K., Dotani, T., Yoshida, A., Vaughan, B. A., & Norris, J. P. 1990, PASJ, 43, 113
Norris, J. P., & Wood, K. S. 1985, IAU Circ., No. 4087
Pennix, W., Lewin, W. H. G., Mitsuda, K., van Paradijs, J., van der Klis, M., & Zijlstra, A. A. 1990, MNRAS, 243, 114
Pozdnyakov, L. A., Sobol, I. M., & Sunyaev, R. A. 1983, Soviet Sci. Rev. E, 2, 189
Schulz, G. M., & Wijers, R. A. M. J. 1993, A&A, 273, 123
Shibazaki, N., Elsner, R., Bussard, R., Ebisuzaki, T., & Weisskopf, M. 1988, ApJ, 331, 247
Shibazaki, N., Elsner, R., & Weisskopf, M. 1987, ApJ, 332, 831
Shibazaki, N., & Lamb, F. 1987, ApJ, 318, 767
Stollman, G. M., Hasinger, G., Lewin, W. H. G., van der Klis, M., & van Paradijs, J. 1987, MNRAS, 227, 7P
Turner, M. J. L., et al. 1989, PASJ, 41, 345
van der Klis, M. 1989a, ARA&A, 27, 517
———. 1989b, in Timing Neutron Stars, ed. H. Ögelman & E. P. J. van den Heuvel (Dordrecht: Kluwer), 27
———. 1991, in Frontiers of X-ray Astronomy, ed. Y. Tanaka & K. Koyama (Tokyo: Universal Academy), 139
van der Klis, M., Hasinger, G., Stella, L., Langmeier, A., Paradijs, J., & Lewin, W. H. G. 1987, ApJ, 319, L13
van der Klis, M., Jansen, F., van Paradijs, J., Lewin, W. H. G., Trümper, J., & Sztajno, M. 1985a, IAU Circ., No. 4043
van der Klis, M., Jansen, F., van Paradijs, J., Lewin, W. H. G., van den Heuvel, E. P. J., Trumper, J., & Sztajno, M. 1985b, Nature, 336, 22
van den Klis, M., Jansen, F., White, N., Stella, L., & Peacock, A. 1985c, IAU Circ., No. 4068
Vaughan, B. A. 1991, Ph.D. thesis, Stanford University
Vrtilek, S. D., Penninx, W., Raymond, J. C., Verbunt, F., Hertz, P., Wood, K., Lewin, W. H. G., & Mitsuda, K. 1991, ApJ, 376, 278
Vrtilek, S. D., Raymond, J. C., Garcia, M. R., Verbunt, F., Hasinger, G., & Kürster, M. 1990, A&A, 235, 162
Wang, Y. M., & Schlickeiser, R. 1987, ApJ, 313, 200
Wijers, R. A. M. J., van Paradijs, J., & Lewin, W. H. G. 1987, MNRAS, 228, 17P
Wood, K. S., Ftaclas, C., & Kearney, M. 1988, ApJ, 324, L63
Wood, K. S., et al. 1991, ApJ, 379, 295